Biochemistry

Identification of a Na⁺-Binding Site near the Oxygen-Evolving Complex of Spinach Photosystem II

Jimin Wang,* Joshua M. Perez-Cruet, Hao-Li Huang, Krystle Reiss, Christopher J. Gisriel, Gourab Banerjee, Divya Kaur, Ipsita Ghosh, Alisha Dziarski, M. R. Gunner, Victor S. Batista, and Gary W. Brudvig*

Read Online

ACCESS | Metrics & More | Article Recommendations

ABSTRACT: The oxygen-evolving complex (OEC) of photosystem II (PSII) is an oxomanganese cluster composed of four redox-active Mn ions and one redox-inactive Ca^{2+} ion, with two nearby bound Cl^- ions. Sodium is a common counterion of both chloride and hydroxide anions, and a sodium-specific binding site has not been identified near the OEC. Here, we find that the oxygen-evolution activity of spinach PSII increases with Na^+ concentration, particularly at high pH. A Na^+-specific binding site next to the OEC, becomes available after deprotonation of the D1-H337 amino acid residue, is suggested by the analysis of two recently published PSII cryo-electron microscopy maps in combination with quantum mechanical calculations and multiconformation continuum electrostatics simulations.

$d = 3.20 \text{ Å}$

Na⁺
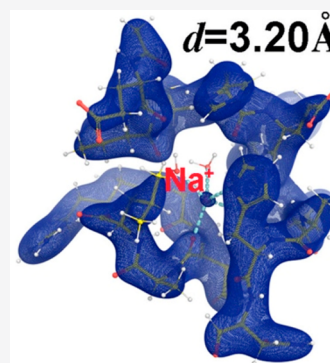
The oxygen-evolving complex (OEC) of photosystem II (PSII) catalyzes the oxidation of water, generating molecular dioxygen (O_2), protons (H^+), and electrons (e^-), during the light-period reactions of photosynthesis:[1−3]

$$2H_2O \rightarrow O_2 + 4e^- + 4H^+$$
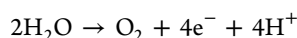
Many simple inorganic salts such as $MnCl_2$, $CaCl_2$, and NaCl modulate the oxygen-evolution ability of PSII, influence the OEC structure, and regulate its activity. Earlier studies of the oxygen-evolution activity of spinach PSII implicitly suggested a possible functional role for sodium in OEC function.[4] For example, oxygen evolution of spinach PSII membranes in MES [i.e., 2-(N-morpholino)ethanesulfonic acid] buffer with $Ca(OH)_2$ produced 100 units (in micromoles of O_2 per milligram of Chl per hour) in the presence of 2 mM NaI, while O_2 evolution was completely suppressed when NaI was removed.[4] However, in NaOH-MES buffer, the level of oxygen evolution increased to 450 units with 2 mM NaI and remained at 250 units without NaI.[4] The upshift in the kinetic profile may have been caused by the estimated 8 mM Na^+ present in the NaOH-containing buffer, suggesting that oxygen evolution is activated at low Na^+ concentrations. Oxygen evolution is inhibited at high Na^+ concentrations because Na^+ becomes competitive with Ca^{2+}; thus, Na^+ likely binds in place of Ca^{2+} in the OEC under these conditions.[5] In contrast, Na^+ also becomes an uncompetitive inhibitor at high Ca^{2+} concentrations, which suggests the presence of another yet-to-be-identified Na^+-specific binding site that may be distal to

the OEC.[5] Uncompetitive inhibition is not observed with other monovalent ions such as K^+, Cs^+, and $[N(CH_3)_4]^+$.

The effects of Na^+ on the PSII activity are complicated and dependent on many conditions, including Ca^{2+} concentration and pH. Na^+ is almost always present as a counterion, and no pH-dependent kinetic studies have been carried out to explicitly determine the potential functional role of Na^+ in oxygen evolution. The crystal structure of *Thermosynechococcus vulcanus* PSII determined at 1.9 Å resolution at pH 6.5 has established the Mn_4CaO_5 OEC structure, with $Mn^{3+/4+}$ and Ca^{2+} as integral components, and two nearby bound Cl^- ions, although Na^+ binding near the OEC has not been identified.[6] The presence of bound Na^+, however, cannot be ruled out because the electron density peaks for Na^+ and H_2O are very similar because both species have the same number of electrons. In contrast, the electrostatic potential (ESP) maps of cryo-electron microscopy (cryo-EM)[7−9] can differentiate Na^+ from H_2O because the scattering factors of cations are much higher than those of neutral species.[10] Thus, we have carefully examined the recently published cryo-EM data to

explore whether we can identify a Na$^+$-binding site. Indeed, the recently published ESP maps of PSII from *Spinacea oleracea* (spinach) and *Pisum sativum* (pea) at pH 7.5[7,8] allow us to identify a Na$^+$-specific binding site adjacent to the OEC near D1-H337. Computational simulations show that sodium binding occurs at high pH when the nearby D1-H337 is deprotonated, with Na$^+$ supplementing the missing positive charge of D1-H337. Consistent with the nature of the proposed binding site, our measurements of oxygen-evolution activity of purified spinach PSII membranes at pH 6.0 and 8.0 show that the addition of Na$^+$ increases oxygen-evolution activity significantly at pH 8.0, but not at pH 6.0.

■ MATERIALS AND METHODS

Preparation of Spinach PSII Membranes and Na$^+$ Depletion. PSII-enriched thylakoid membrane fragments were prepared from spinach as previously described and suspended in a buffer containing 15 mM NaCl, 20 mM MES, and 30% (v/v) ethylene glycol.[11−13] The pH was adjusted to 6.0 with NaOH. Suspended and purified PSII membranes were stored in liquid nitrogen. Sodium was removed from PSII membranes by washing with a Na$^+$-depleted buffer. The PSII sample was homogenized, centrifuged, and resuspended three times with the Na$^+$-depleted buffer to decrease the Na$^+$ concentration by >50-fold. The Na$^+$-depleted buffer contained 20 mM CaCl$_2$, 20 mM MES, and 20 mM HEPES [4-(2-hydroxyethyl)-1-piperazineethanesulfonic acid], and the pH was adjusted to 6.0 using N(CH$_3$)$_4$OH to prevent the introduction of any monovalent metal ions. Each wash was followed by centrifugation (Sorvall SS-34 rotor, 4 °C, 36,600g, 20 min), and the pellet was collected. The Na$^+$-depleted PSII membranes were then suspended in 17.5 mM CaCl$_2$, 17.5 mM MES, 17.5 mM HEPES, and 30% (v/v) ethylene glycol. The pH of the suspension buffer was adjusted to 6.0 using N(CH$_3$)$_4$OH.

Oxygen Assay of Na$^+$-Depleted PSII Membranes. The oxygen-evolution activity of the Na$^+$-depleted PSII membranes was measured using a Clark-type O$_2$ electrode as previously described.[11−14] The assay buffers were prepared at 0, 10, 20, and 40 mM NaCl and contained 20 mM CaCl$_2$ (i.e., ≥40 mM Cl$^-$), 20 mM MES, and 20 mM HEPES. The pH was adjusted to 6.0 and 8.0 using N(CH$_3$)$_4$OH. Both 1 mM K$_3$[Fe(CN)$_6$] and 0.25 mM PPBQ (phenyl-p-benzoquinone) were used as electron acceptors. The chlorophyll concentration for the assay was 3.8 μg/mL. The oxygen-evolution activity assay was also performed at pH 8 in the presence of either 40 mM N(CH$_3$)$_4$Cl and 0 mM NaCl or 0 mM N(CH$_3$)$_4$Cl and 40 mM NaCl with a fixed total Cl$^-$ concentration of 80 mM to rule out Cl$^-$ activation.

Density Functional Theory (DFT) Geometry Optimization for ESP Calculations. ESP maps were calculated for a 250-atom model taken from the 3ARC/5V2C Protein Data Bank (PDB) structure of PSII,[6,13] including D1-[M329-N338], D2-[R348-L352], and two water molecules (D1-370 and D2-381), both of which were free to move during DFT geometry optimization. A Na$^+$ complex ion was inserted into the binding pocket with as many H$_2$O ligands as possible, which were also free to move during optimization. In these Na$^+$-containing models, D1-H337 was deprotonated. In Na$^+$-free models, D1-H337 was treated separately as both deprotonated and protonated at its Nδ1 position. DFT geometry optimization was performed using a B3LYP functional of the Gaussian 2016 software package with the 6-31G basis set for C, N, and H

atoms and the 6-31G(d) basis set for O, S, and Na$^+$ atoms.[15,16] ESP maps were generated using the Merz−Singh−Kollman scheme.[17,18]

The corresponding atomic charges were derived from ESP maps, and charge-only Coulomb ESP maps were recalculated using the DelPhi program.[19,20] Inside the protein boundary, the macroscopic dielectric constant was set to 4 or 1, whereas that of the solvent continuum was always set to 80. These ESP maps were Fourier inverted using the Phenix software suite to obtain the corresponding structure factors.[21] The maps were recalculated using structure factors with appropriate Wilson B-factors on spacing grids corresponding to a fixed 0.18 Å resolution with varying reciprocal resolution using CCP4.[22] This calculation was performed in two sets of grid spacing after adding Wilson B-factors of 41.3 and 64.6 Å^2 to the structure factors. The first set of spacing is fixed at an effective resolution of 0.18 Å, and the second set varies with effective resolutions of 2.5 and 3.2 Å. The effective resolution of the van der Waals (vdW) component of cryo-EM maps was estimated using an empirical relationship obtained for X-ray crystallographic data sets:[23]

$$\ln(B) = 2.0548 - 1.8169 \ln(S_{max})$$

where B is the Wilson B-factor of the diffraction data and S_{max} is the maximum reciprocal resolution. The accuracy of both electron density and ESP peaks is dependent on the real-space grid resolution that is used to sample corresponding functions for exactly the same structure factors.

Multiconformer Continuum Electrostatics (MCCE) Sampling. MCCE sampling computes the Boltzmann distribution of all protonation states for the Asp, Glu, His, Lys, and Arg side chains, His tautomers, and terminal water molecules bound to the OEC.[24−26] It finds the Na$^+$-binding site(s) starting with the DFT quantum mechanics/molecular mechanics (QM/MM) optimized structure, including 137 residues within 15 Å of the OEC (∼2500 atoms) in the S$_1$ state.[27] The dielectric constant was set to 4 for the protein and 80 for the solvent. Electrostatic interactions and solvation energies were calculated with the program DelPhi as implemented in MCCE, using Parse charges and radii in the presence of 150 mM implicit salt. Grand Canonical Monte Carlo (GCMC) sampling was repeated for the OEC fixed in the S$_1$ (3443) state, i.e., with [Mn(1)]$^{3+}$, [Mn(2)]$^{4+}$, [Mn(3)]$^{4+}$, and [Mn(4)]$^{3+}$. The Amber force field was used for non-electrostatic Lennard-Jones energies.[24−26] Water molecules were removed. The IPECE (Implement Protein Environment for Continuum Electrostatics) algorithm was used to add 262 Na$^+$ ions into all cavities, within an 8 Å radius of D1-H337.[24] The ions were then subjected to GCMC sampling, during which each can freely leave the protein while residue protonation states can also change. The equilibrium binding of Na$^+$ to the protein was calculated as a function of the Na$^+$ relative chemical potential between pH 6 and 9.[26]

■ RESULTS AND DISCUSSION

pH-Dependent Na$^+$ Activation of the Oxygen-Evolution Activity of Spinach PSII Membranes. Oxygen evolution was fast at pH 6.0 but considerably slower at pH 8.0 at the same Na$^+$ concentration (Figure 1A), which is consistent with a previous study.[28] However, in the presence of 40 mM Na$^+$ at pH 8, oxygen evolution is 2−3-fold faster compared to that of Na$^+$-depleted PSII (Figure 1). At the optimal pH of 6.0 for spinach PSII activity, there is only a slight increase in the
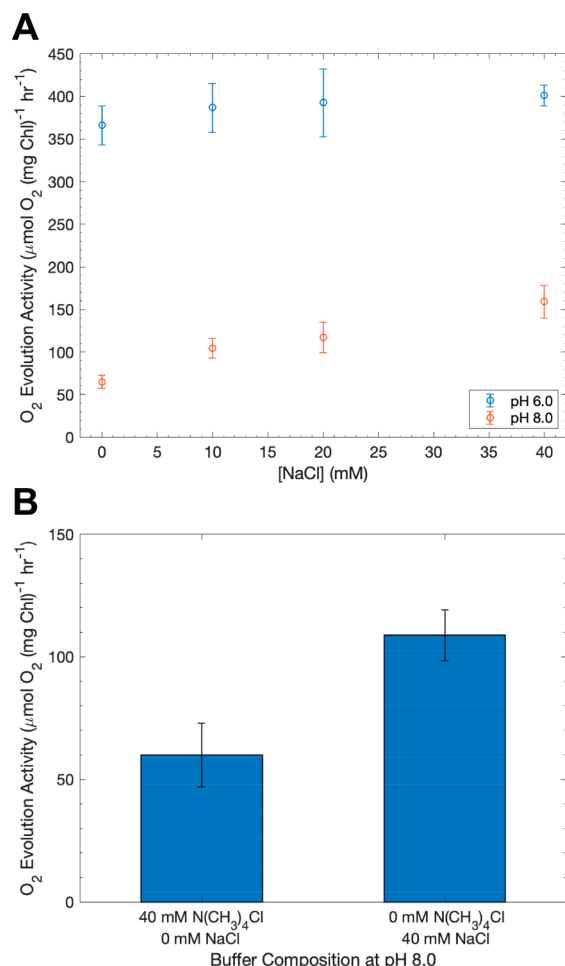
Figure 1. Na$^+$ dependence of PSII. The oxygen-evolution activity of Na$^+$-depleted PSII membranes is shown as a function of varying NaCl concentration and pH. (A) At pH 8 with N(CH$_3$)$_4$Cl, but no NaCl, very low oxygen-evolution activity is observed (red). With the addition of NaCl, oxygen-evolution activity is increased to >100 μmol of O$_2$ (mg Chl)$^{-1}$ hr^{-1}. At pH 6, the high OEC activity shows a weaker NaCl dependence (blue). (B) Activities in the presence of either 40 mM N(CH$_4$)$_4$Cl or 40 mM NaCl showing that Cl$^-$ does not activate oxygen evolution at pH 8.0. Averaged activities (micromoles of O$_2$ per milligram of Chl per hour) with standard deviations (error bars) from three or more assays are shown.

activity with an increase in Na$^+$ concentration (Figure 1). At pH 8.0, Cl$^-$ activation is ruled out because the rate of oxygen evolution remains low when NaCl is substituted with an equal concentration of N(CH$_3$)$_4$Cl (Figure 1B). Earlier measurements always included 15 mM NaCl to maintain a sufficiently high chloride concentration for optimal oxygen evolution so that the Na$^+$ dependence was hidden.[26] At a low pH, [N(CH$_3$)$_4$]$^+$ was shown to have no effect on the oxygen-evolution activity of NaCl-washed thylakoid membranes where PSII lacked extrinsic subunits.[5] In this study, extrinsic proteins are preserved; therefore, it is unlikely that [N(CH$_3$)$_4$]$^+$ could bind near the active site to impact oxygen evolution. Thus, we ascribe the observed difference in activity at pH 8 to the Na$^+$ concentration. On the basis of our current pH-dependent oxygen-evolution activity results, we anticipated that ligands of this Na$^+$-binding site might include an ionizable group with a pK_a within the experimental pH range of 6−8, such as a His residue.

Our study shows that Na$^+$ is required for the optimal oxygen-evolution activity of spinach PSII, and that this activation is most pronounced at higher pH values. These effects are difficult to observe when either the pH or the Na$^+$ concentration is not varied individually. This study does not directly distinguish between active and passive modes of activation. In a passive mode, Na$^+$ would simply play an essential role in maintaining the structural integrity of PSII at higher pH values where it is especially fragile. In an active mode, Na$^+$ would accelerate one of the slow steps of oxygen evolution. At high pH values, some extrinsic subunits may be partially dissociated. This dissociation should not affect the Na$^+$-dependent activation of oxygen evolution observed here. We have not examined additional roles of Na$^+$ at higher concentrations in this study, which could be more complicated because it can bind many more sites.

Identification of a Na$^+$-Specific Binding Site from Recent Cryo-EM Maps. Two cryo-EM maps were recently reported at ∼3.2 Å resolution for plant PSII supercomplexes (with light-harvesting complex II) at pH 7.5, one from spinach (EMD 6617/PDB 3JCU) (Figure 2) and the other from pea
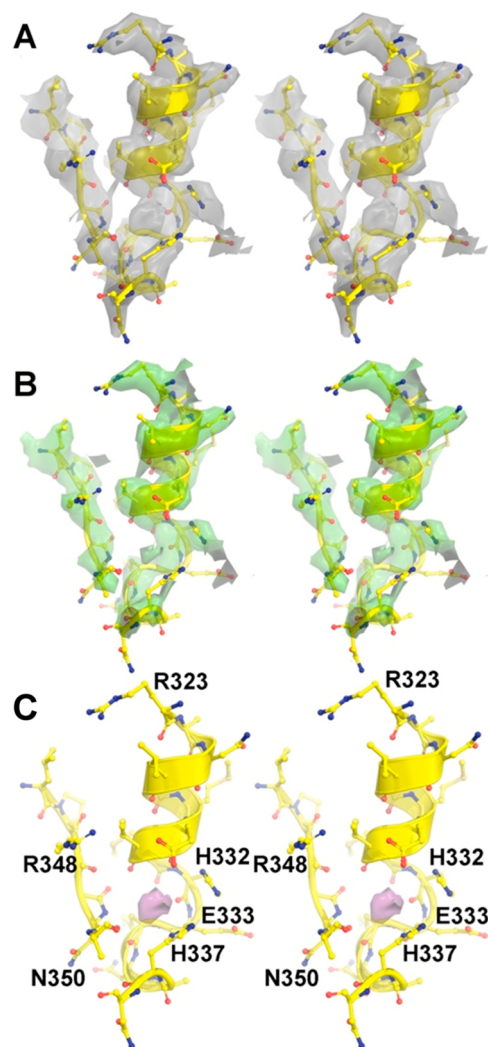

Figure 2. Stereodiagram views of the 3JCU coordinates superimposed onto the cryo-EM map of EMD-6617 contoured at (A) 3.5σ, (B) 4.5σ, and (C) 4.0σ (for Na$^+$ only, ESP features for the remaining protein atoms have been omitted for the sake of clarity).

(EMD 6742/PDB 5XNM).[7,8] These maps were examined for a Na$^+$-specific binding site near the OEC to provide a structural basis for the pH-dependent Na$^+$-specific activation of spinach PSII observed here. We are aware that the actual pH of the cryo-EM samples may differ from the cited values due to the freezing process.

An examination of the two cryo-EM maps revealed an unexplained positive peak of approximately spherical symmetry inside a pocket (Figures 2 and 3).[7,8] Map sharpening routinely carried out for cryo-EM maps can produce artifacts,[29] especially in an extreme case when dynamic experimental electric potential (EP) maps are converted to ESP maps by setting the underlying B-factors to zero and by making the amplitudes of the corresponding structure factors independent of resolution. We have verified that the peak we observed in the cryo-EM map is not an artifact of map sharpening. A similar positive peak is present after a Laplacian operation on the original, unsharpened cryo-EM maps, which produces locally distributed charge density (CD) maps without introducing any artifacts (Figure 3A,B).[30]
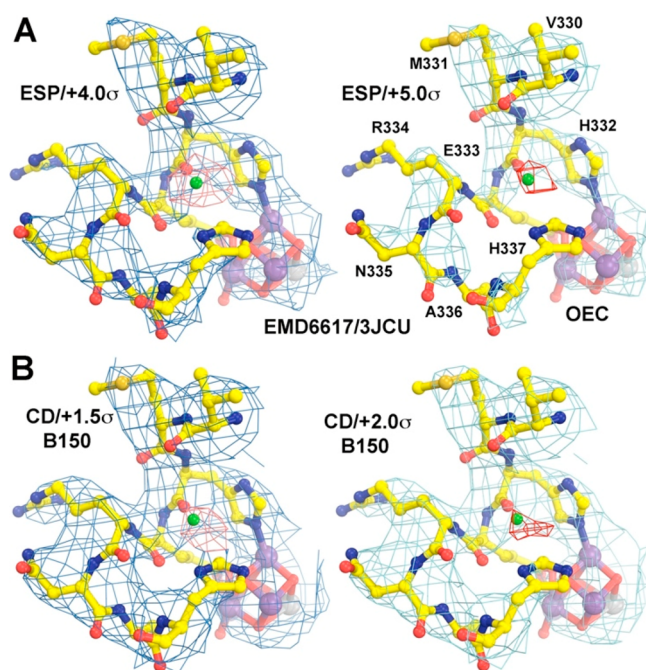

Figure 3. Single, well-isolated, approximately spherically symmetric peak observed in the cryo-EM map (EMD 6617) recently reported for spinach PSII (PDB 3JCU) at the putative Na$^+$-binding site. (A) Two contouring levels (left, 4.0σ; right, 5.0σ) of the EMD 6617 map. (B) Two contouring levels (left, 1.5σ; right, 2.0σ) of the unsharpened CD map.

In both of the cryo-EM maps, the ESP value of this peak is higher than that of its ligands, including D1-H337 and other surrounding protein residues, suggesting that a positively charged species occupies this site (Figures 2 and 3). We assign this positive peak to a Na$^+$ ion, which is the only monovalent cation present in the buffer of the protein samples imaged.[7,8] This putative Na$^+$-binding pocket is ~7.6 and 9.5 Å from the two Cl$^-$ ions near the OEC and ~7.6 Å from Mn1 of the OEC.[6] This pocket is located at the C-terminus of a D1 α-helix and corresponds to the pocket occupied by two ordered water molecules (water-370 and water-381) in the 1.9 Å resolution

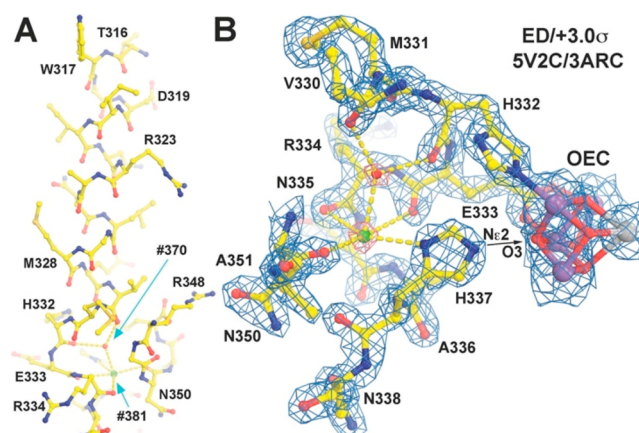crystal structure of *T. vulcanus* PSII determined at pH 6.5 (Figure 4).[6]

Figure 4. Corresponding location of the Na$^+$-binding pocket (observed in the spinach PSII cryo-EM structure) in the X-ray structure of *T. vulcanus* PSII (PDB 3ARC/5V2C). (A) Locations of water-381 (green, Na$^+$ in spinach PSII) and water-370 (red) at the C-terminus of a long transmembrane α-helix. (B) Electron density map contoured at 3.0σ using the re-refined 3ARC model (5V2C) showing that the peak of water-381 is slightly larger than that of water-370, due to a small difference in the atomic B-factor. Nε2 of D1-H337 is hydrogen bonded to O3 of the OEC.

There are two possible interpretations for an ESP peak with such a large peak maximum. One is a Na$^+$ ion with a formal charge of +1. The other is that two water molecules may be merged together to exhibit a single positive ESP peak. However, an analysis of a DFT-derived ESP map excludes the second interpretation while supporting the first interpretation (see Figures 5−7). We have verified that the two water molecules in the *T. vulcanus* PSII crystal structure (pH 6.5) are not a mis-identified Na$^+$ ion because when water-370 was replaced with Na$^+$ in a DFT-calculated ESP map, its atomic B-factor value refined during model refinement was larger than those of atoms with which it interacts by ~7 Å^2. With a water molecule at this position, there was no difference in atomic B-factors among all interacting atoms in this area, implying that the water molecule is correctly assigned.

Evidence of pH-Dependent Na$^+$ Binding from Recent Cryo-EM Maps. Two additional cryo-EM structures were reported at lower pH values (5.7 and 6.5) and higher resolution (~2.7 Å),[8,9] which provide direct evidence for pH-dependent binding of Na$^+$ to D1-H337. These structures of PSII purified at these two lower pH values differ from that at pH 7.5. At pH 7.5, the Na$^+$ ion is seen to bind to D1-H337 (EMD 6741/PDB 5XNM) in the pea PSII supercomplexes, which are arranged in an unstacked configuration. However, at pH 5.7 in a stacked configuration (EMD 6742/PDB 5XNL), D1-H337 is likely to be protonated, and two water molecules were observed to bind in this pocket in an arrangement that is almost identical to the high-resolution cyanobacterial PSII crystal structure at pH 6.5.[6,8] At pH 6.5, an additional cryo-EM structure (EMD 9955/PDB 6KAC) at 2.7 Å resolution was computationally extracted from the supercomplex PSII structure from the green alga *Chlamydomonas reinhardtii*.[9] In that structure, there is a single resolved ESP peak in the pocket, which differs from the cyanobacterial PSII crystal structure at the same pH.[6,9] The maximum for this lone peak is much
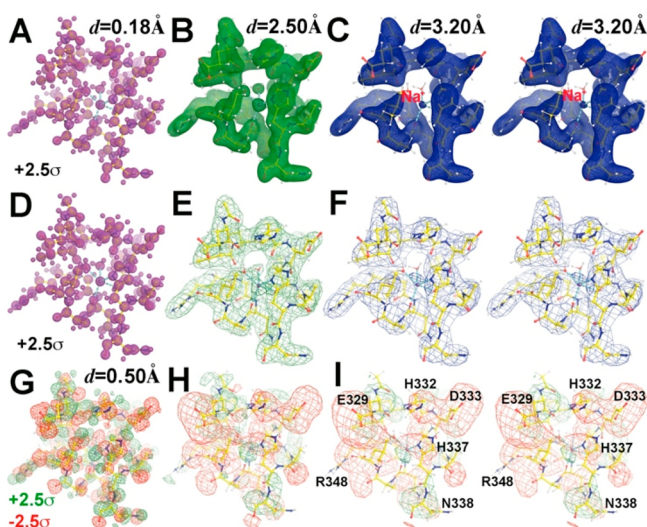
Figure 5. DFT-derived theoretical EP and DelPhi-calculated EP functions of the first atom model with Na$^+$ bound and deprotonated D1-H337. (A−F) DFT-derived EP maps. (G−I) DelPhi-calculated EP maps. The right two panels are stereodiagrams (C, F, and I). First row (A−C) with increasing atomic motions ($\Delta B = 0$; first panel at 0.18 Å resolution; second panel with $\Delta B = 41.3$ Å^2 at ~2.50 Å resolution; third panel with $\Delta B = 64.6$ Å^2 at ~3.20 Å resolution) but with the fixed real-space supersampling at 0.18 Å resolution. The map is contoured at 2.5σ. The second row is the same as the first row in reciprocal spacing but with reduced real-space grid sampling (which is approximately corresponding to their reciprocal space resolution). The third row is the Delphi-calculated EP function contoured at 2.5σ (green) and −2.5σ (red) with the same reciprocal resolutions as the first row, but with fixed grid spacing corresponding to 0.50 Å resolution.

smaller than that found at pH 7.5 relative to ESP peaks for D1-H337. It is likely that under these conditions, D1-H337 is partially deprotonated, and that the observed single ESP peak corresponds to a mixture of both Na$^+$- and water-occupied binding pockets.

Utilizing Charge Properties in Experimental Cryo-EM Maps. Cryo-EM maps display the spatial variation of ESP, which is the sum of the Coulombic and van der Waals (vdW) potentials at each point.[31−33] The ESP peak for a cation is more easily visualized than that of a neutral atom because the net positive partial charge generates an extra positive Coulomb ESP that augments the underlying vdW EP peak.[34] The ESP peak of an anion is less easily visualized than that of a neutral atom because the net negative partial charge generates an extra negative Coulomb EP function that diminishes the underlying vdW EP peaks.[33] These charge effects make the ESP peak of Na$^+$ more conspicuous than those of Cl$^-$ and H$_2$O (i.e., Na$^+$ > H$_2$O > Cl$^-$). This simple principle is useful for an initial identification of ions in cryo-EM maps. This expectation is met in that both cryo-EM maps published for spinach PSII[7,8] exhibit no isolated positive peak corresponding to the two known Cl$^-$ ions. The authors of those studies probably retained the Cl$^-$ ions in their starting model from an extrapolation of the previously determined X-ray structures of cyanobacterial PSII.[6] The X-ray crystallographic electron density peak of Cl$^-$ is more easily visualized than that of Na$^+$ because Cl$^-$ has nearly twice the number of electrons of Na$^+$, whereas the electron density peaks of Na$^+$ and H$_2$O are difficult to distinguish because these species have the same number of electrons, i.e., Cl$^-$ ≫ H$_2$O ∼ Na$^+$. This highlights the importance of considering charges for the proper interpretation of cryo-EM maps in this resolution range.

Cryo-EM ESP maps can be viewed as the convolution products of static ESP maps with dynamic motions (i.e., B-factors), which include a time average of large numbers of macromolecules frozen at different time points of the trajectory, as well as measurement errors. DFT calculations were used to generate theoretical static ESP maps from the accurate atomic coordinates obtained using X-ray crystallography, which can be compared with experimental data only after properly adding the atomic motion described by the Wilson B-factor. However, when ESP maps are calculated using atomic scattering factors, the Coulomb and the vdW ESP components are separated. The charges used for calculation of the Coulomb maps are derived from the DFT-derived total ESP map. The charge-only Coulomb ESP map can then be recalculated using DelPhi, which provides a finite difference solution to the Poisson−Boltzmann equation, with appropriate Wilson B-factors added (Figure 5G−I).[19,20]

The charge-only ESP map shows the following. (1) Na$^+$ has a large positive ESP at its nuclear position. (2) The O atom of H$_2$O has a negative ESP. (3) H atoms of H$_2$O have only very weak effects on the ESP at the O position. The sum of these contributions makes the total ESP value, which corresponds to the experimental ESP value at the nuclear position of Na$^+$, much larger than that of neutral H$_2$O species, assuming the same small atomic motions of the two species (Figure 5C,D). The differences between one Na$^+$ ion and two water molecules become smaller with an increase in the level of atomic motion. However, the summed ESP values of H$_2$O molecules disappear below the noise level before that of Na$^+$ at any given contouring level. Given the typical H$_2$O−H$_2$O distance of ~2.8 Å, ESP peaks of two H$_2$O molecules will never merge into a single elongated peak with an increase in the level of atomic motion before their peaks disappear below the noise level. Thus, the single ESP peak inside the putative Na$^+$-binding pocket observed in the two cryo-EM maps reported for spinach PSII[7,8] cannot be assigned as two merged H$_2$O molecules, but only as a Na$^+$ cation or a partially hydrated Na$^+$ complex ion because Na$^+$ is the only monovalent cation present in the buffer of these protein samples.[7,8]

The contribution of a Coulomb component to the cryo-EM map, which we did not include in an estimation of the local resolution, can greatly alter the appearance of ESP peaks for both cations and anions.[33,34] This makes it unreliable to use the appearance (i.e., the apparent spatial resolution) of electron density maps for a comparison with the appearance of cryo-EM maps to calibrate their effective resolution (i.e., the underlying B-factors), as suggested recently.[35] At ~3.2 Å, one can definitely identify the binding of Cl$^-$ in electron density maps but not in cryo-EM maps. One can definitely identify Na$^+$ in cryo-EM maps, but it is nearly impossible in electron density maps at medium resolution. These contrasting features of electron density maps and cryo-EM maps can be reproduced using both DFT calculation as done in this study and electron scattering factors published for a small set of ions with integral charge numbers.[36]

Ligand Assignment in the Hydrated Complex Na$^+$ Cation Using DFT. While we can qualitatively identify the isolated positive peak observed in the two cryo-EM maps at pH 7.5 as a bound Na$^+$ cation on the basis of its net charge of +1, the map at ~3.2 Å resolution does not provide sufficient information to fully determine its specific H$_2$O ligands and

coordination geometry. In such a case, the ligands and coordination geometry may be proposed upon combining the experimental information from the cryo-EM maps with physicochemical principles.

We calculated DFT-ESP maps for three atomic models directly derived from the X-ray crystallography structure of cyanobacterial PSII and chose the one that is the most consistent with the cryo-EM maps. In the first model, we inserted a hydrated Na^+ complex into several initial binding sites with as many H_2O ligands as possible and let DFT optimize the coordination geometry, assuming that D1-H337 is deprotonated (Figure 5). The second and third atomic models feature protonated and deprotonated D1-H337, respectively, and include two water molecules (W370 and W381 as in 3WU2/5V2C) but not Na^+ (Figures 6 and 7).[6,13]
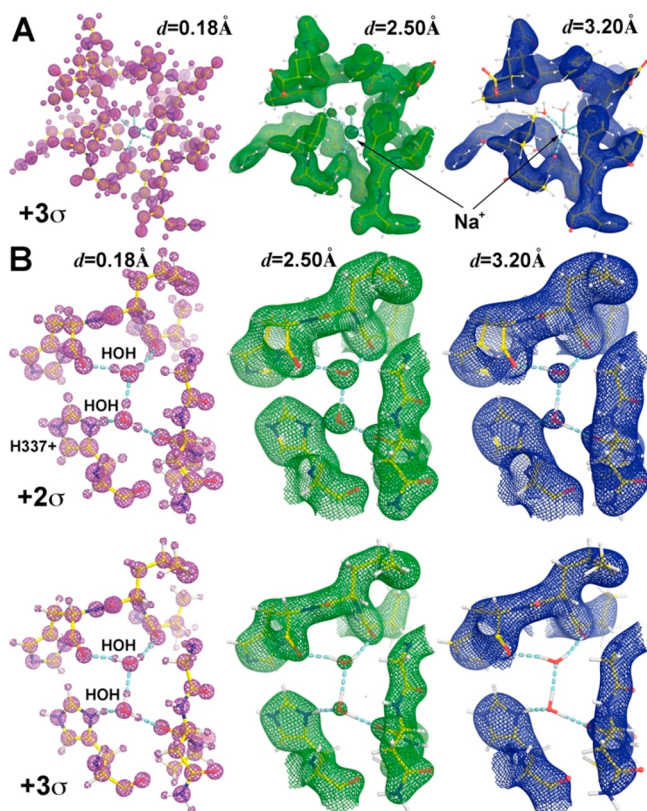

Figure 6. DFT QM/MM model of the second atomic model with two water molecules and protonated D1-H337. (A) Same as panels A−C of Figure 5 but contoured at 3.0σ. (B) DFT-derived EP function for two H_2O molecules bound as in the *T. vulcanus* PSII crystal structure, contoured at 2σ (middle row) and 3σ (bottom row) with atomic motions included as indicated.

The DFT models were built by using the OEC optimized in the S_1 state in cyanobacterial PSII. All H atoms of the water ligands are explicitly modeled with no rotational disorder of torsional angles of any kind. Spinach PSII, analyzed in this work, and cyanobacterial PSII are highly conserved in sequence. Although they have different pH−kinetic profiles, these differences can be assigned to a replacement of D1-A87 in spinach PSII with D1-N87 in cyanobacterial PSII near the OEC.[14] This residue is ~15 Å from the putative Na^+-binding site, and there is no difference in the protein sequence near the Na^+-binding site; therefore, we assume that this should not affect our DFT calculations of Na^+ binding.
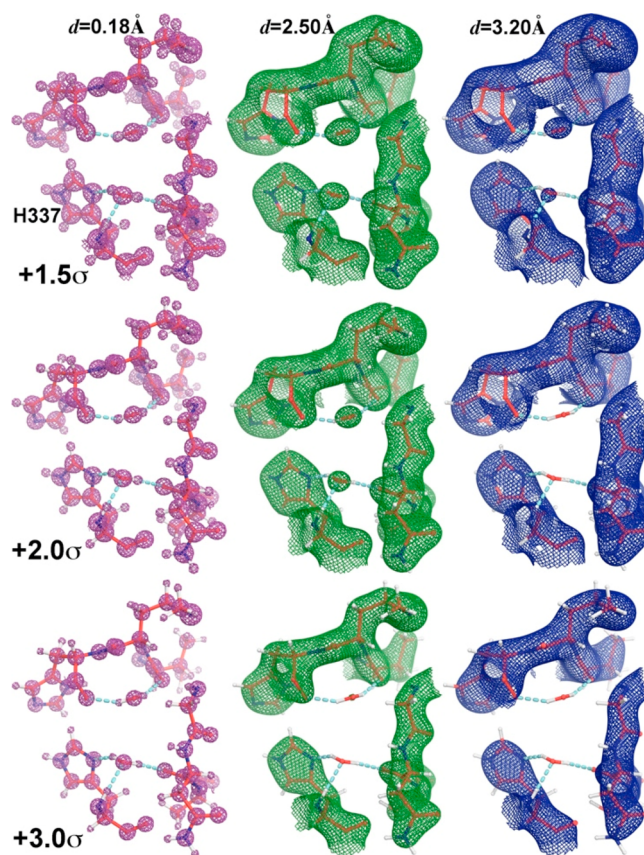

Figure 7. DFT-derived theoretical ESP function for the third model with two H_2O molecules bound as in the *T. vulcanus* PSII crystal structure with protonated D1-H337, contoured at 1.5σ (top row), 2σ (middle row), and 3σ (bottom row) with atomic motions included as indicated.

After DFT optimization, the first Na^+-bound atomic model matched the cryo-EM maps better than either of the two Na^+-free atomic models (Figures 5−7). The Na^+-binding pocket, buried inside the protein, appears to be only large enough to accommodate a maximum of three water ligands to the bound Na^+. Two protein ligands of the Na^+ ion are the deprotonated D1-H337 side chain and the D2-N350 backbone carbonyl (Figure 8A,B). Effectively, a partially hydrated $[Na(H_2O)_3]^+$ complex ion replaces the two water molecules (W370 and W381) found inside the binding pocket of the crystal structure of *T. vulcanus* PSII.[6,13] The mean Na^+ coordination bond length in our DFT model is 2.40 ± 0.13 Å, varying from 2.24 to 2.61 Å. The small size of this binding pocket may prevent larger K^+ and Cs^+ monovalent cations from binding. Neither K^+ nor Cs^+ ion exhibits noncompetitive inhibition as Na^+ does.[5] Nor have they been tested to see if they enhance oxygen-evolution activity at high pH. The pentavalent coordination geometry also rules out binding of NH_4^+. These stipulations support the presence of a highly specific Na^+-binding pocket.

In our DFT-optimized structure, one water ligand is almost precisely superimposed onto the water designated as W370 in the cyanobacterial structure 5V2C.[6,13] It retains the same pattern of H bonding interactions with the D1 protein that is found in the crystal structure. The two other new water molecules functioning as Na^+ ligands (Z1 and Z2 water Na^+ ion) also have three and two H bonds with the protein, respectively (Figure 8A,B, green dashes). Both Z1 and Z2 form
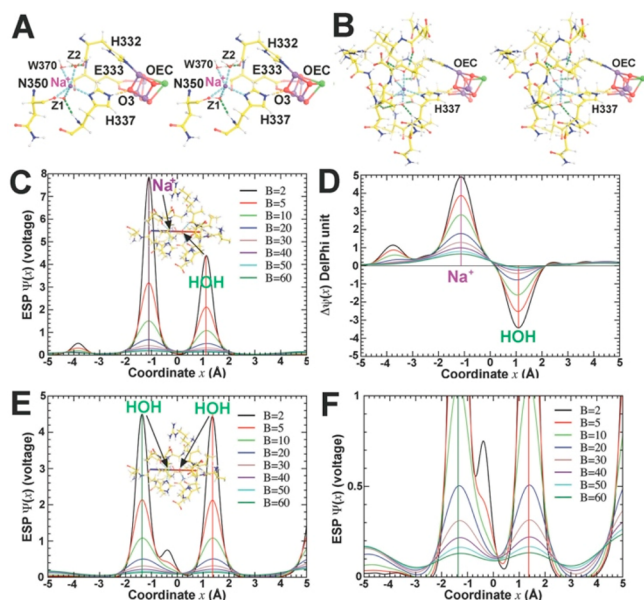
Figure 8. DFT-optimized Na^+-bound structure of spinach PSII and molecular mechanical basis for EP disparity between Na^+ and HOH in the Na^+-specific binding pocket. (A) Na^+ coordination geometry in stereodiagram. Its ligands include three water molecules (W370 and two new water molecules named Z1 and Z2), the D1-H337 side chain, and the D2-N350 backbone carbonyl group. D1-H337 is H bonded to O3 of the OEC. (B) Zoomed-out stereodiagram view showing how three water molecule ligands are held in place in the Na^+-binding pocket. (C) DFT-derived EP functions plotted along the Na^+/water-370 axis on the absolute voltage scale as a function of B-factor [i.e., effective resolution (see the text)]. (D) DelPhi-calculated charge-only Coulomb potentials along the Na^+/water-370 axis. (E) DFT-derived EP functions plotted along the water-381/water-370 axis on the absolute voltage scale as a function of B-factor. (F) Close-up view of panel E.

H bonds with D1-protein residues, and Z1 also interacts with D2-N350. With the three H bonds, the Z1 O atom has perfect tetrahedral interaction geometry (Figure 8B).

Deprotonation of D1-H337 and pH-Dependent Binding of Na^+. Cryo-EM maps correspond to the ensemble of configurations of microstates in the frozen samples, and their corresponding thermal fluctuations are sampled during the cryo-EM imaging. We have analyzed an ensemble of protein microstates with and without Na^+ using GCMC as implemented in MCCE.[24,25] MCCE will bring the protonation states of all amino acids into equilibrium with the cofactor redox states at the defined pH and relative Na^+ chemical potential with a background ionic strength of 150 mM. The full PSII complex can be analyzed in MCCE.[26] Here, 137 residues near the OEC in the S_1 state were simulated.[27]

Our MCCE simulations of the protonation states of amino acid residues in the cyanobacterial PSII structure show that there is a single high-affinity Na^+-binding site near D1-H337. In the absence of Na^+, D1-H337 is protonated between pH 6.5 and 9.0, while it always remains neutral in the presence of Na^+. Thus, the protonation state of D1-H337 is dependent on the pH and Na^+ concentration. At a given pH, an increasing Na^+ concentration leads to both Na^+ binding and deprotonation of D1-H337.[26] Previous experimental and computational data have shown that D1-337 must be protonated at low pH values for the OEC to function properly.[37,38] At higher pH values, it is easier to deprotonate the His, so the Na^+ affinity increases.

Because of the competition between H^+ and Na^+, the calculated Na^+ affinity increases 10-fold/pH unit as the pH is increased from 6 to 9.

The high pK_a for D1-H337 and the ability of Na^+ to replace the His cation at higher pH values reflect the affinity for a cation in this region of PSII. The backbone dipoles as well as the nearby bound Cl^- and D1-Asp61 contribute a negative Coulomb potential that favors the positive charge. The summed contribution of the OEC and its primary protein ligands affect the cation affinity by <1 kcal/mol. In displacing water ligands of the hydrated $[Na(H_2O)_6]^+$ complex ion, we see that the protein can provide higher-affinity ligands, making it a specific Na^+-binding site. Although either a deprotonated His side chain or a carboxylate could serve as a ligand for Na^+, our calculation shows that neither alone provides sufficient interaction energy for binding of Na^+. In PSII, the Na^+-specific binding pocket is located at the C-terminus of a long α-helix, and this helix has a cumulative negative ESP that originates from the aligned dipoles of the backbone carbonyls.[39] At low pH values, this negative ESP stabilizes protonated D1-H337, whereas at high pH values, it stabilizes the bound Na^+ that binds when D1-H337 is deprotonated.

Environmental Factors for Modeling of the Na^+-Binding Site. Two notable long-range environmental factors observed in PSII, which have been omitted from this study, could affect the absolute EP value of Na^+ and its H_2O ligands as found in additional DFT calculations. These factors include long-range ESP contributions from the aligned dipole moments of backbone carbonyls of the long D1 α-helix (Figure 4A). The Na^+-binding pocket is located at the C-terminus of the D1 helix and is subject to the cumulative effects of aligned dipole moments.[40] In addition, partial occupancy of the OEC in the PSII samples imaged, which may be due to partial loss during electron scattering,[41,42] will affect the ESP nearby. However, it is likely that these long-range ESP effects are similar regardless of whatever species occupies the Na^+-binding pocket. Therefore, these factors do not alter the overall conclusion about the relative ESP magnitude of Na^+ and H_2O.

■ CONCLUSION

In this study, we have identified a possible Na^+-specific binding site immediately adjacent to the OEC at high pH values, next to deprotonated D1-H337. Na^+ binding is consistent with recently reported cryo-EM maps, our DFT QM/MM and MCCE calculations, and our kinetic measurements of oxygen-evolution activity of spinach PSII as a function of both Na^+ concentration and pH. We suggest that Na^+ binding upon deprotonation of D1-H337 allows for the conservation of charge near the OEC and helps to fine-tune a wide pH range for oxygen-evolution activity.

■ ASSOCIATED CONTENT

Accession Codes
PSII protein D1 (PSII-D1, PSII-A), psbA, P69560. PSII CP-47 (PSII-CP47, PSII-B), psbB, P04160. PSII CP-43 (PSII-CP43 or P6, PSII-C), P06003. PSII protein D2 (PSII-D2, PSII-D), P06005. PSII cytochrome b_{559} α (reaction center V, PSII-E), P69383. PSII cytochrome c_{559} β (reaction center VI, PSII-F), P60128. PSII reaction center H (PSII-H), P05146. PSII reaction center I (PSII-I), P62103. PSII reaction center J (PSII-J), Q9M3L2. PSII reaction center K (PSII-K), P12163. PSII reaction center M (PSII-M), P62112. PSII reaction center L (PSII-L), P60150. PSII Mn-stabilizing protein O (PSII-O),

P12359. PSII reaction protein T (PSII-T), P61840. PSII reaction center YCF12 (PSII-Y), P80470. PSII reaction center Z (PSII-Z), Q9M3M6. PSII reaction center W (PSII-W), Q41387.

■ AUTHOR INFORMATION

Corresponding Authors

Jimin Wang − *Department of Molecular Biophysics and Biochemistry, Yale University, New Haven, Connecticut 06520-8114, United States;* ⓘ orcid.org/0000-0002-4504-8038; Email: jimin.wang@yale.edu

Gary W. Brudvig − *Department of Molecular Biophysics and Biochemistry and Department of Chemistry, Yale University, New Haven, Connecticut 06520-8114, United States;* ⓘ orcid.org/0000-0002-7040-1892; Email: gary.brudvig@yale.edu

Authors

Joshua M. Perez-Cruet − *Department of Chemistry, Yale University, New Haven, Connecticut 06520-8107, United States*

Hao-Li Huang − *Department of Chemistry, Yale University, New Haven, Connecticut 06520-8107, United States*

Krystle Reiss − *Department of Chemistry, Yale University, New Haven, Connecticut 06520-8107, United States*

Christopher J. Gisriel − *Department of Chemistry, Yale University, New Haven, Connecticut 06520-8107, United States*

Gourab Banerjee − *Department of Chemistry, Yale University, New Haven, Connecticut 06520-8107, United States*

Divya Kaur − *Department of Physics, City College of New York (CCNY), New York, New York 10031, United States; Department of Chemistry, The Graduate Center of the City University of New York, New York, New York 10016, United States*

Ipsita Ghosh − *Department of Chemistry, Yale University, New Haven, Connecticut 06520-8107, United States*

Alisha Dziarski − *Department of Chemistry, Yale University, New Haven, Connecticut 06520-8107, United States*

M. R. Gunner − *Department of Physics, City College of New York (CCNY), New York, New York 10031, United States; Department of Chemistry, The Graduate Center of the City University of New York, New York, New York 10016, United States*

Victor S. Batista − *Department of Chemistry, Yale University, New Haven, Connecticut 06520-8107, United States;* ⓘ orcid.org/0000-0002-3262-1237

Complete contact information is available at:
https://pubs.acs.org/10.1021/acs.biochem.0c00303

Author Contributions

J.M.P.-C. and H.-L.H. contributed equally to this work. J.W., G.W.B., V.S.B., and M.R.G. conceived the concept and designed experiments for this study. J.M.P.-C., H.-L.H., C.J.G., G.B., and I.G. performed biochemical studies. K.R. performed DFT calculations. D.K. carried out MCCE calculations. J.W. analyzed cryo-EM maps. All co-authors contributed to writing the manuscript.

Notes

The authors declare no competing financial interest.

■ ABBREVIATIONS

PSII, photosystem II; OEC, oxygen-evolving complex; cryo-EM, cryo-electron microscopy; ESP, electrostatic potential; EP, electric potential; vdW, van der Waals; MES, 2-(*N*-morpholino)ethanesulfonic acid; HEPES, 4-(2-hydroxyethyl)-1-piperazineethanesulfonic acid; PPBQ, phenyl-*p*-benzoquinone.

■ REFERENCES

(1) Vinyard, D. J., Ananyev, G. M., and Dismukes, G. C. (2013) Photosystem II: the reaction center of oxygenic photosynthesis. *Annu. Rev. Biochem.* 82, 577−606.

(2) Vinyard, D. J., and Brudvig, G. W. (2017) Progress toward a molecular mechanism of water oxidation in photosystem II. *Annu. Rev. Phys. Chem.* 68, 101−116.

(3) Askerka, M., Brudvig, G. W., and Batista, V. S. (2017) The O_2-evolving complex of photosystem II: Recent insights from quantum mechanics/molecular mechanics (QM/MM), extended X-ray absorption fine structure (EXAFS), and femtosecond X-ray crystallography data. *Acc. Chem. Res.* 50, 41−48.

(4) Bryson, D. I., Doctor, N., Johnson, R., Baranov, S., and Haddy, A. (2005) Characteristics of iodide activation and inhibition of oxygen evolution by photosystem II. *Biochemistry* 44, 7354−7360.

(5) Waggoner, C. M., Pecoraro, V., and Yocum, C. F. (1989) Mono-valent cations (Na^+, K^+, Cs^+) inhibit calcium activation of photosynthetic oxygen evolution. *FEBS Lett.* 244, 237−240.

(6) Umena, Y., Kawakami, K., Shen, J. R., and Kamiya, N. (2011) Crystal structure of oxygen-evolving photosystem II at a resolution of 1.9 A. *Nature* 473, 55−60.

(7) Wei, X., Su, X., Cao, P., Liu, X., Chang, W., Li, M., Zhang, X., and Liu, Z. (2016) Structure of spinach photosystem II-LHCII supercomplex at 3.2 Å resolution. *Nature* 534, 69−74.

(8) Su, X., Ma, J., Wei, X., Cao, P., Zhu, D., Chang, W., Liu, Z., Zhang, X., and Li, M. (2017) Structure and assembly mechanism of plant $C_2S_2M_2$-type PSII-LHCII supercomplex. *Science* 357, 815−820.

(9) Sheng, X., Watanabe, A., Li, A., Kim, E., Song, C., Murata, K., Song, D., Minagawa, J., and Liu, F. (2019) Structural insights into light harversting for photosystem II in green algae. *Nature Plants* 5, 1320−1330.

(10) Peng, L. M. (1999) Electron atomic scattering factors and scattering potentials of crystals. *Micron* 30, 625−648.

(11) Berthold, D. A., Babcock, G. T., and Yocum, C. F. (1981) A highly resolved, oxygen-evolving photosystem II from spinach thylakoid membranes: EPR and electron-transport properties. *FEBS Lett.* 134, 231−234.

(12) Beck, W. F., de Paula, J. C., and Brudvig, G. W. (1985) *Biochemistry* 24, 3035−3043.

(13) Wiwczar, J. M., LaFountain, A. M., Wang, J., Frank, H. A., and Brudvig, G. W. (2017) Chlorophyll a with a farnesyl tail in thermophilic cyanobacteria. *Photosynth. Res.* 134, 175−182.

(14) Banerjee, G., Ghosh, I., Kim, C. J., Debus, R. J., and Brudvig, G. W. (2018) Substitution of the D1-Asn(87) site in photosystem II of cyanobacteria mimics the chloride-binding characteristics of spinach photosystem II. *J. Biol. Chem.* 293, 2487−2497.

(15) Becke, A. D. (1993) Density-functional thermochemistry. III. The role of exact exchange. *J. Chem. Phys.* 98, 5648−5652.

(16) Marenich, A. V., Cramer, C. J., and Truhlar, D. G. (2009) Universal solvation model based on solute electron density and on a continuum model of the solvent defined by the bulk dielectric constant and atomic surface tensions. *J. Phys. Chem. B B113*, 6378−6396.

(17) Singh, U. C., and Kollman, P. A. (1984) An approach to computing electrostatic charges for molecules. *J. Comput. Chem. 5*, 129−145.

(18) Besler, B. H., Merz, K. M., and Kollman, P. A. (1990) Atomic charges derived from semiempirical methods. *J. Comput. Chem. 11*, 431−439.

(19) Honig, B., and Nicholls, A. (1995) Classical electrostatics in biology and chemistry. *Science 268*, 1144−1149.

(20) Nicholls, A., and Honig, B. (1991) A rapid finite-difference algorithm, utilizing successive over-relaxation to solve the Poisson-Boltzmann equation. *J. Comput. Chem. 12*, 435−445.

(21) Adams, P. D., Afonine, P. V., Bunkoczi, G., Chen, V. B., Davis, I. W., Echols, N., Headd, J. J., Hung, L. W., Kapral, G. J., Grosse-Kunstleve, R. W., McCoy, A. J., Moriarty, N. W., Oeffner, R., Read, R. J., Richardson, D. C., Richardson, J. S., Terwilliger, T. C., and Zwart, P. H. (2010) PHENIX: a comprehensive Python-based system for macromolecular structure solution. *Acta Crystallogr., Sect. D: Biol. Crystallogr. D66*, 213−221.

(22) Winn, M. D., Ballard, C. C., Cowtan, K. D., Dodson, E. J., Emsley, P., Evans, P. R., Keegan, R. M., Krissinel, E. B., Leslie, A. G., McCoy, A., McNicholas, S. J., Murshudov, G. N., Pannu, N. S., Potterton, E. A., Powell, H. R., Read, R. J., Vagin, A., and Wilson, K. S. (2011) Overview of the CCP4 suite and current developments. *Acta Crystallogr., Sect. D: Biol. Crystallogr. D67*, 235−242.

(23) Wang, J. (2017) Experimental charge density from electron microscopic maps. *Protein Sci. 26*, 1619−1626.

(24) Song, Y., Mao, J., and Gunner, M. R. (2003) Calculation of proton transfer in bacteriorhodopsin in bR and M intermediates. *Biochemistry 42*, 9875−9888.

(25) Song, Y., and Gunner, M. R. (2009) Using multiconformation continum electrostatics go compare chloride-binding motifs in alpha-amylase, human serum albumin, and Omp32. *J. Mol. Biol. 387*, 840−856.

(26) Song, Y., Mao, J., and Gunner, M. R. (2009) MCCE2: improving protein pKa calculations with extensive side chain rotamer sampling. *J. Comput. Chem. 30*, 2231−2247.

(27) Askerka, M., Wang, J., Brudvig, G. W., and Batista, V. S. (2014) Structural changes in the oxygen-evolving complex of photosystem II induced by the S_1 to S_2 tranition: a combined XRD and QMMM study. *Biochemistry 53*, 6860−6822.

(28) Lee, C. I., and Brudvig, G. W. (2004) Investigation of the functional role of Ca^{2+} in the oxygen-evolving complex of photosystem II: A pH-dependence study of the substitution of Ca^{2+} by Sr^{2+}. *J. Chin. Chem. Soc. 51*, 1221−1228.

(29) Vilas, J. L., Vargas, J., Martinez, M., Ramirez-Aportela, E., Melero, R., Jimenez-Moreno, A., Garduno, E., Conesa, P., Marabini, R., Maluenda, D., Carazo, J. M., and Sorzano, C. O. S. (2020) Re-examining the spectra of macromolecules. Current practice of spectral quasi B-factor flattening. *J. Struct. Biol. 209*, 107447.

(30) Wang, J. (2017) Experimental charge density from electron microscopic maps. *Protein Sci. 26*, 1619−1626.

(31) Wang, J., and Moore, P. B. (2017) On the interpretation of electro microscopic maps of biological macromolecules. *Protein Sci. 26L*, 122−129.

(32) Wang, J. (2017) On the appearance of carboxylates in electrostatic potential maps. *Protein Sci. 26*, 396−402.

(33) Wang, J. (2017) On contribution of known atomic partial charges of protein backbone in electrostatic potential density maps. *Protein Sci. 26*, 1098−1104.

(34) Wang, J., Liu, Z., Frank, J., and Moore, P. B. (2018) Identification of ions in experimental electrostatic potential maps. *IUCrJ 5*, 375−381.

(35) Wlodawer, A., Li, M., and Dauter, Z. (2017) High-resolution cryo-EM maps and models: A crystallographer's perspective. *Structure 25*, 1589−1597.

(36) Peng, L. M. (1998) Electron scattering factors of ions and their parameterization. *Acta Crystallogr., Sect. A: Found. Crystallogr. A54*, 481−485.

(37) Nakamura, S., and Noguchi, T. (2017) Infrared determination of the protonation state of a key histidine residue in the photosynthetic water oxidizing center. *J. Am. Chem. Soc. 139*, 9364−9375.

(38) Pantazis, D. (2020) Evaluation of new low-valent computational models for the oxygen-evolving complex of photosystem II. *Chem. Phys. Lett. 753*, 137629.

(39) Mobley, D. L., and Gilson, M. K. (2017) Predicting binding free energies: frontiers and benchmarks. *Annu. Rev. Biophys. 46*, 531−558.

(40) Wang, J., Videla, P. E., and Batista, V. S. (2017) Effects of aligned alpha-helix peptide dipoles on experimental electrostatic potentials. *Protein Sci. 26*, 1692−1697.

(41) Wang, J., Reiss, K., Brudvig, G. W., and Batista, V. S. (2018) Reduced occupancy of the oxygen-evolving complex of photosystem II detected in cryo-electron microscopy maps. *Biochemistry 57*, 5925−2929.

(42) Wang, J., Liu, Z., Crabtree, R. H., Frank, J., and Moore, P. B. (2018) On the damage done to the structure of the Thermoplasma acidophilum proteasome by electron radiation. *Protein Sci. 27*, 2051−2061.